Anisotropic effect of an external magnetic field on non-equilibrium concentration fluctuations in nanoparamagnetics

ANA OPRISAN
College of Charleston
Dept. Physics and Astronomy
66 George St., Charleston, SC 29424
U.S.A.
oprisana@cofc.edu

ASHLEY RICE
College of Charleston
Dept. Physics and Astronomy
66 George St., Charleston, SC 29424
U.S.A.
riceae@g.cofc.edu

GABRIELLE SEYMORE
College of Charleston
Dept. Physics and Astronomy
66 George St., Charleston, SC 29424
U.S.A.
seymoregp@g.cofc.edu

Abstract: We performed two shadowgraph-based experiments using superparamagentic nanocolloids to investigate the effect of a horizontal magnetic field on the intensity of concentration - enhanced non-equilibrium fluctuations (c-NEFs). The experiments were performed on Earth with a concentration gradient oriented vertically upward under the influence of a horizontal (perpendicular to the concentration gradient) external magnetic field. We used a shadowgraph method to record c-NEFs and a differential dynamic algorithm (DDA) to investigate quantitatively the changes in the structure factor and the correlation time of c-NEFs. We found that the diffusion coefficient transiently decreases when the magnetic field is turned on/off presumably due to the formation/destruction of paramagnetic clusters.

Key–Words: Diffusion and aggregation, magnetic nanoparticles, complex fluids, thermodynamics of non-equilibrium processes

1 Introduction

Non-equilibrium Fluctuations in Nanocolloids. Spontaneous mass transfer in liquid mixtures [26, 51, 52] and colloidal suspensions [6, 33, 53] can be driven by concentration inhomogeneity. Light scattering experiments have beed used for visualization of fluctuations of thermodynamic parameters.

In opposite to systems at macroscopic thermodynamic equilibrium, out-of equilibrium, refractive index fluctuations in the bulk of fluids rising from fluctuations of thermodynamic variables are long-ranged and enhanced. These two properties make the so-called non-equilibrium fluctuations detectable by techniques using a pixelated detection unit such as shadowgraphy [53, 9, 12, 7, 24, 40].

The coupling between velocity fluctuations parallel to the driving gradient and the macroscopic concentration gradient [58, 43] enhance non-equilibrium fluctuations (c-NEFs). On Earth, the scale of long-ranged c-NEFs is quenched by gravity [58, 44, 23, 5, 38, 39, 37], viscosity forces [9, 12, 14, 30], and to some extent by the confinement effect [41, 25]. Under microgravity conditions, only the confinement limits the intensity of fluctuations [6, 33, 53, 45, 35, 36, 57]. Concentration-enhanced non-equilibrium fluctuations have been used, for example, for accurate measurement of transport coefficients in nanocolloids [10, 17, 24, 15, 31]. Long-ranged, c-NEFs have been

experimentally observed in isothermal binary mixtures under a time-dependent concentration gradient [9, 12]. Their structure factor scales with k^{-4} at large wavenumbers, where $k = \frac{4\pi n_0}{\lambda_0} \sin\left(\frac{\theta}{2}\right)$ is the wavenumber of the scattered light, n_0 is the refractive index of the optical medium, λ_0 is the vacuum wavelength of the light source, and θ is the scattering angle [53, 9, 12].

Magnetic Nanocolloids. Nanocolloidal suspensions of magnetic particles have recently received significant attention, for example, as potential drug carriers [46, 2, 21, 19] and for water and wastewater treatment. In uniform magnetic fields, magnetic nanoparticles in colloidal suspensions aggregate and form nanorod-like structures [20, 4] that are tunable and have no permanent magnetization.

In this paper, we further expanded on our previous experiments performed with the same nanocolloids under a vertical magnetic field [40], by analyzing c-NEFs during the free-diffusion of colloidal suspensions of superparamagnetic Fe_2O_3 nanoparticles against pure water both in the absence and in the presence of a horizontal external magnetic field. We performed two different experiments using the same sample cell and concentration gradient. In both experiments we used the same magnetic field intensity. In the first experiment, initially the magnetic field was off and we only recorded free diffusion fluctuations,
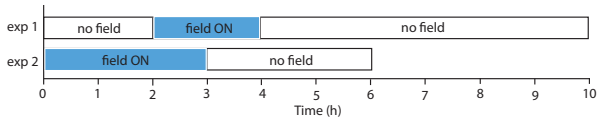
Figure 1: **Experimental protocol.** The first experiment had three sequences: it started only with the initial concentration gradient and no magnetic field, followed by a sequence with a horizontal magnetic field turned on, and ended with no magnetic field again. The second experiment had only two sequences: it started with the same concentration gradient as in experiment 1 and a horizontal magnetic field turned on, and ended with no magnetic field.

then the magnetic field was turned on, and finally the field was turned off again (see the three sequences of "exp 1" in Fig. 1). The second experiment began with the magnetic field on, and then the field was removed (see the two sequences of "exp 2" in Fig. 1). The first 1-2 hours in both experiments are affected by very long wavelength fluctuations of the interface during the initial stage of setting the concentration gradient [9, 12]. For this reason, we used the method of image variance (see below and also [24]) to remove such images (see the hashed regions in Fig. 1).

We used a shadowgraph method to visualize local refractive index fluctuations that induce measurable light intensity fluctuations of the scattered light parallel to the concentration gradient (see Fig. 2 of the experimental setup). We extracted both the product of the structure factor $S(k,t)$ by the transfer function of the shadowgraph method $T(k)$, i.e. $S(k,t)T(k)$, and the correlation time $\tau(k,t)$ of c-NEFs from the scattered light intensity [9, 38, 13].
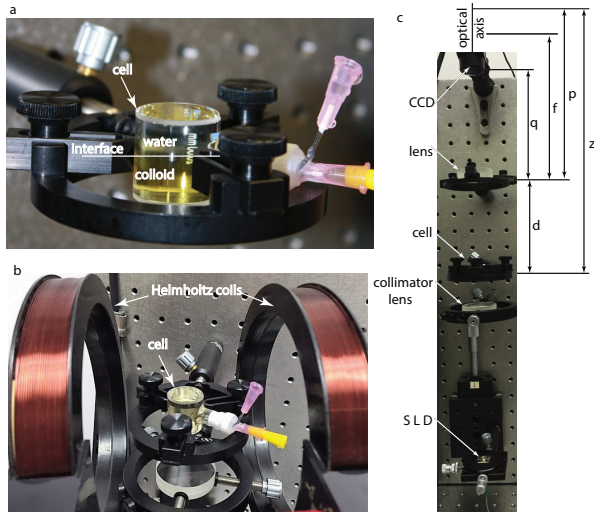
2 Experimental Setup

The experimental setup was previously described in great details (see [40]). Briefly, an initial concentration gradient was prepared by layering pure water over the nanocolloid suspension in isothermal conditions (see Fig. 2a). During the free-diffusion process, the initial concentration gradient decreases and the diffusion process ends when the homogeneous state is reached. The diffusion time $\tau_d = h^2/(4\pi D)$ were $h = 2\,\mathrm{cm}$ is the height of the cell and D is the diffusion coefficient. Stokes-Einstein equation $D = k_B T/(6\pi\eta r)$ gives a rough estimation of the diffusion coefficient, where $\eta = 10^{-3}$ N s/m^2 (for water at room temperature) is the dynamic viscosity and $r = 10\,\mathrm{nm}$ is the radius of the spherical particles. As a result, $D \approx 2.210^{-7}$ cm^2/s and $tau_d \approx 10^6$

s. We used the same superparamagnetic nanocolloid purchased from Sciventions Inc. as in [40] with a concentration of 1.5 mg/ml and particle diameters in the range of 1-10 nm. The nanocolloid was contained by a Hellma 120-OS-20 cylindrical glass cell (see also [38, 39, 40] for more detailed descriptions of similar experimental setups). At room temperature, the magnetization curve of this superparamagnetic nanocolloid is linear and non-hysteretic [50]. During the experiments, a horizontal (perpendicular to the concentration gradient) magnetic field of $4.2\,\mathrm{mT}$ was turned on by using a pair of Teltron Helmholtz Coils from 3B Scientific (320 turns, $138\,\mathrm{mm}$ coil diameter) as shown in Fig. 2b. The beam from a monochromatic light source with a wavelength of $\lambda_0 = 760\,\mathrm{nm}$ (Superlum Ireland Co., SLD-261) was collimated with an achromatic doublet to uniformly illuminate the diffusion cell. The fluctuations of the refractive index were recorded with a progressive scan SONY XCL-X700 CL CCD camera with a resolution of 1024 pixels $\times$ 768 pixels, a sensor area of $5.8\,\mathrm{mm} \times 4.92\,\mathrm{mm}$, and pixel resolution of $4.65\,\mu\mathrm{m}$ (see Fig. 2c). Both experiments were recorded at one frame per second, which is significantly smaller than the correlation time of fluctuations to allow a reasonable accuracy of image processing. A similar experimental setup with one collimating lens between the light source and the sample cell and one relay lens between the sample cell and the CCD camera was used, for example, by Vailati et al. (see Fig. 3 for a schematic diagram of the prototype apparatus and Fig. 5 for a diagram of the experimental setup [56]). The setup in [56] is also an Intra Focal Shadowgraph (IFS) similar to our setup shown in Fig. 2.

3 Image Processing

Shadowgraph method allows measurements of the refractive index fluctuations by recombining the strong transmitted light beam with the weak scattered light from the sample [55]. The resultant phase shift of the interference patterns depends both on the wavenumber and the sample-recording plane distance. Assuming long wavelength fluctuations, the product between the static structure factor $S(k,t)$ of the sample and the shadowgraph transfer function $T(k)$ can be obtained by Fourier analysis of the interference pattern [55, 11]. Although the static shadowgraph technique was pioneered in 1990s by Wu et al [59], the dynamic shadowgraph was only recently applied to measuring the autocorrelation function of non-equilibrium concentration fluctuations in free diffusion and thermodiffusion experiments [9, 12, 24, 25, 13, 11].

Square images $I(\vec{x}, t)$ of 512 pixels $\times$ 512 pix-

Figure 2: **The shadowgraph experimental setup for a free diffusion experiment in horizontal magnetic field.** (a) The sample cell unit was filled with a superparamagentic nanocolloid (bottom half) and water (top half). (b) The cell is placed between two Helmholtz coils that created a horizontal uniform magnetic field at cell's location. (c) From the bottom to the top of the vertical optical bench we aligned a fiber optic that comes from a superluminscent diode (SLD), a collimator lens, the sample cell, followed by a focusing lens, and a CCD camera. The achromatic doublets have a focal length of $f = 20$ cm and a diameter of 4 cm. For our experimental conditions the distance between the naonocolloid-water interface and the image plane was $z \approx 50$ cm.

els allowed the visualization of an actual image size at the CCD sensor of $w_{sensor} = 512$ pixels $\times 4.65\,\mu$m $= 2.4$ mm. For our optical setup, the distance from the center of the sample cell to the relay (focusing) lens is $d \approx 13$ cm, the distance from the relay lens to the CCD camera was $q \approx 15$ cm, and the focal length of the lens was $f = 20$ cm. Because $q < f$ our experimental setup belongs to the Intra Focal Shadowgraph (IFS) [9, 56]. Based on lens' maker formula $1/p + 1/q = 1/f$ and the definition of magnification $m = q/p$, it results that the magnification of our setup was $m = q/f - 1 \approx$ -0.35. Similarly, the distance to the image plane was $p = f(1 + 1/m) \approx -37$ cm (see Fig. 2c). As a result, the effective distance z from the sample to the plane focused onto the CCD was $z = d - p \approx 50$ cm. Using the ratio of image versus object sizes $m = w_{sensor}/w$ it results that our measurements cover a square with a side of about $w = w_{sensor}/m = 6.8$ mm of the 2 cm diameter of the diffusion cell. In the Fourier space, this object size corresponds to a minimum wavenumber of $k_{min} = 2\pi/w \approx 9.24$ cm^{-1}.

We used a Differential Dynamic Algorithm (DDA) to analyze the recorded data (see [9, 12, 38, 37, 40, 13, 11] for more detailed descriptions of this image processing algorithm). Briefly, each image $I(\vec{x}, t)$ was normalized by dividing it by its average value, i.e. $i(\vec{x}, t) = I(\vec{x}, t)/\langle I(\vec{x}, t)\rangle_{\vec{x}}$, in order to reduce the effect of variable light intensity (similar procedure has been used, for example, by [9, 12, 13]). The brackets $\langle \ldots \rangle$ indicate averaging operation and the subscript $\vec{x}$ indicates that the average is over the spatial location of image pixels. The light intensity modulations were extracted from the difference between normalized images at several delay times Δt, i.e. $\delta i(\vec{x}, t, \Delta t) = i(\vec{x}, t) - i(\vec{x}, t + \Delta t)$, with the resultant subtracted image $\delta i(\vec{x}, t, \Delta t)$ defined as the fluctuation image (see Fig. 3a1,b1,c1).

The DDA algorithm uses the Fourier transform of image difference, or fluctuation image, $\delta i(\vec{x}, t, \Delta t)$, i.e. $\delta i(\vec{k}, t, \Delta t) = \mathcal{F}(\delta i(\vec{x}, t, \Delta t))$, to compute the power spectra $\delta i(\vec{k}, t, \Delta t)^2$ shown in Fig. 3a2, b2, and c2.

If the images are too close, as in the case of successive frames with $\Delta t = 1$ s, then there is a significant overlap between the images and thus producing only a small change in the signal. As a result, the difference $\delta i(\vec{x}, t, \Delta t)$ of the two images contains almost no usable signal (see Fig. 3a1, b1, and c1). Conversely, images too far apart are almost statistically independent and the difference $\delta i(\vec{x}, t, \Delta t)$ contains no useful information regarding the correlation time of fluctuations. Therefore, to capture the correlation time of fluctuations we scanned a wide range of delay
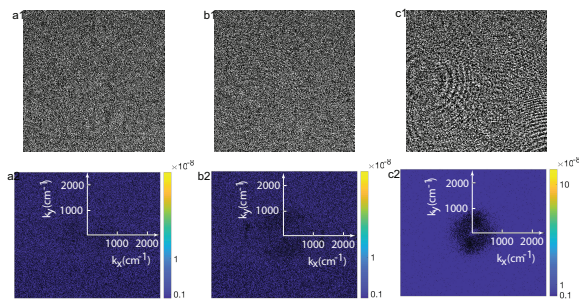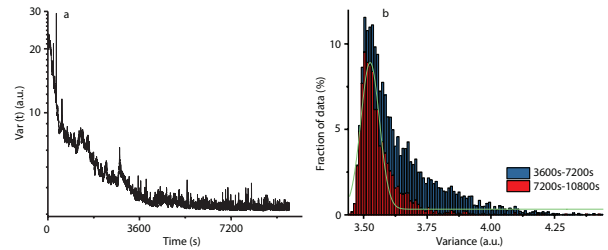
Figure 4: **Variance of successive images.** (a) The variance of images $I(\vec{x}, t)$ recorded for the first 1-2 hours is very large due to the presence of very long wavelength fluctuations at the interface during the initial stage of setting the concentration gradient [9, 12]. (b) The corresponding histograms for the second and third hour of the recordings with the variance shown in panel (a). The fit of the histogram for the third hour with a Gaussian function gives a standard deviation of 0.0367 ± 0.002 for the variance (see continuous line curve).

Figure 3: **Normalized differences between shadowgraph images and their corresponding power spectra.** The difference images $\delta i(\vec{x}, t, \Delta t)$ between images with a delay of (a1) $\Delta t = 1$ second, (b1) $\Delta t = 10$ second, and (c1) $\Delta t = 100$ second. For each normalized image difference $\delta i(\vec{x}, t, \Delta t)$, the power spectrum shows no structure for delays shorted than 100 s (see a2 and b2) and a clear symmetric structure for delay times in the range of the correlation time of fluctuations (c2). The axes of the power spectrum plots represent wave numbers (k_x, k_y) in cm^{-1} and the colorbar next to each plot shows the power in arbitrary units.

times Δt (see Fig. 3a1,b1, and c1). Some examples of power spectra are shown in Fig. 3a2, b2, and c2. The power spectra show no structure if the the delay time Δt is too short (see Fig. 3a2,b2). For delay times in the range of the correlation time of fluctuations we observed the characteristic ring structure of the power spectra (see Fig. 3c2).

We also implemented an offline pre-processing of acquired images as described in [24]. The purpose of pre-processing was to detect "problematic" images and eliminate them from subsequent computations. The method used in [24] computes the variance of two successive images separated by a delay time Δt, i.e.

$$Var(t) = \langle [I(\vec{x}, t) - I(\vec{x}, t + \Delta t)]^2 \rangle_{\vec{x}},$$

where the average is over the spatial location.

A plot of the variance versus time reveals images that change significantly from one time step to the next, presumably due to dust particle moving in the beam path of the optical set-up [24], vibrations of optical table, etc. The images that are outside three times the root mean square (RMS) value of the variance are associated with a zero weight and therefore eliminated from further processing. The variance algorithm pointed to the same set of "problematic" images both with the original images $I(\vec{x}, t)$ and with the corresponding normalized counterparts $i(\vec{x}, t)$.

As it has been emphasized by Croccolo et al. [9, 12], the initial recordings after the nanocolloid was injected into the sample cell are affected by very long wavelength fluctuations at the interface. Indeed, from Fig. 4a we also noticed that this regime of very large

variances lasts about 1-2 hours and, to our knowledge, such data have always been discarded. The histograms of the variance for the second and the third hour of recording, respectively, show a significant reduction in large variances over time (see Fig. 4b). Although the histograms are asymmetric, we fitted the histogram of variances during the third hour of the experiment with a Gaussian function to get a rough estimate of the standard deviation of variance. The fitting equation was $y_0 + ae^{-0.5((x-b)/c)^2}$, where $y_0 = 0.003 \pm 0.001$ is the offset, $a = 0.085 \pm 0.004$ is the amplitude of Gauss function, $b = 3.526 \pm 0.002$ is the center of the peak, and $c = 0.037 \pm 0.002$ is the standard deviation, or RMS, of the Gaussian fit. We used three times the RMS of the Gaussian fit as our measure for eliminating "problematic" images from subsequent data processing (see [24] for a more detailed description of the variance-based method).

Average Fourier power spectra $\langle \delta i(\vec{k}, t, \Delta t)^2 \rangle_N$ were computed over sets of $N = 512$ image with the same fixed delay time Δt (see [12, 13] for a more detailed description of the algorithm). As we notice from Fig. 3c2, the power spectra and their corresponding averages over a set of $N = 512$ image differences have azimuthal symmetry, which allowed us to use the azimuthal average of the average power spectrum, i.e. $\langle \delta i(\vec{k}, t, \Delta t)^2 \rangle_{N, |\vec{k}|}$, for subsequent calculations. The brackets $\langle \ldots \rangle$ indicate averaging operation and the subscripts $N, |\vec{k}|$ indicate that the average is both over the number of images N and azimuthally over constant wavenumber values $|\vec{k}|$. The azimuthal average $\langle \delta i(\vec{k}, t, \Delta t)^2 \rangle_{N, |\vec{k}|}$ shows the average power (over N sets of image differences) at every magnitude of the vavenumber k for a fixed delay Δt at a given time t.

While the azimuthal average of power spectra shows the evolution of the power versus the magnitude of the wavenumber k at a fixed value of the delay time Δt, at a fixed wavenumber k and different values of the delay times Δt, the time-dependent structure function $C_m(k, t, \Delta t)$ presents the same information regarding the power distribution over a range of delay times Δt for a fixed wavenumber k. $C_m(k, t, \Delta t)$ is related to the time-dependent structure factor $S(k, t)$, the temporal autocorrelation function $G(k, t, \Delta t)$, and the background noise $B(k, t)$ as follows [12, 38, 13, 11, 14]:

$$C_m(k, t, \Delta t) = 2[S(k, t)T(k)(1 - G(k, t, \Delta t)) + B(k, t)], \quad (1)$$

where the shadowgraph transfer function is given by

$$T(k) = 4\sin^2(k^2 z/(2k_0)), \quad (2)$$

where z is the distance from the sample cell to the plane imaged onto the CCD camera (in our experi-

ments $z \approx 50\,\text{cm}$) and $k_0 = 2\pi/\lambda_0$ is the vacuum wavenumber of the incident light. We used Eq. 2 that provides a mathematical formula valid for an infinitely thin sample, but also see [17] for an empirical correction that accounts for a finite sample thickness. A similar transfer function $T(k)$ was used by Vailati et al. [56] for a similar experimental setup that also included a collimating lens and a relay lens (see, for example, Figs. 4 and 6 of [56] for a plot of the above $T(k)$ transfer function). For a more complete treatment of shadowgraph method and more complex forms of $T(k)$ see [55, 11].

By fitting the radial average of the time-dependent structure function $C_m(k, t, \Delta t)$ with equation (1), we determined the product $S(k, t)T(k)$ (see Fig. 5), the intermediate scattering function $G(k, t, \Delta t)$ (see Fig. 6), and the background fluctuations $B(k, t)$. We used OriginLab software that implemented a Levenberg-Marquardt (M-L) a nonlinear curve fitting algorithm, which is particular versatile when estimating uncertainties for and correlations between pairs of fit variables. The optimization function for M-L algorithm is the χ^2, for which we set a 99.99% confidence level to determine an acceptable value of χ^2 [3, 48]. Therefore, by investigating the change in the radial average of the power spectra, i.e. the time-dependent structure function, for different delay times it is possible to extract information about the correlation time, $\tau(k, t)$, of fluctuations.

For giant concentration fluctuations, it has been shown that the theoretical structure factor is given by:

$$S(k, t) = \frac{S_0}{1 + (k/k_c)^4}, \quad (3)$$

where S_0 is the limit of $S_{eq}(\frac{\nabla c}{\nabla c_g} - 1)$ for very small wave vectors k, where S_{eq} is the equilibrium static structure factor value, ∇c is the concentration gradient and ∇c_g is the baro-diffusion-concentration gradient, and k_c is the critical wavenumber (see [9, 12, 13, 56] and references therein for more detailed mathematical expressions for each term). For wavenumbers larger than the critical value k_c the c-NEFs are dominated by diffusion whereas for smaller wavenumbers the gravity [1, 6, 5, 12, 10, 24] and confinement [8, 15, 16, 25] effects dominate. In Fig. 5a we have shown the experimentally computed product $S(k, t)T(k)$ as described above using DDA (see the squares in Fig. 5a) and also the theoretical structure factor given by Eq. 3 (continuous line). The error bars for data fitting were determined with the Levenberg-Marquardt nonlinear curve fitting algorithm set at a 99.99% confidence level to finding an acceptable value of the optimization function χ^2 [3, 48].

We notice from Fig. 5a that for wavenumbers

larger than the cutoff (critical) wavenumber k_c, the structure factor, which is the square modulus of the intensity of c-NEFs [9], decays as k^{-4}, which would indicate that larger c-NEFs are more intense than smaller c-NEFs [58]. For smaller wavenumbers, the fluctuations are quenched by gravity or confinement. In order to capture the observed oscillations in the experimental $S(k,t)T(k)$ obtained with DDA (see the squares in Fig. 5b) we compared them against the product of the theoretical structure factor given by Eq.3 and the transfer function given by Eq. 2 (see continuous line in Fig. 5b). At low wavenumbers, the experimental points follow the slow oscillations of the theoretical $S(k,t)T(k)$ expression, whereas at larger wavenumbers the fast oscillations of the $sin^2(\dots)$ theoretical function given by Eq. 2 are smoothed out (see also [9] for similar results). However, in the log-log plot shown in Fig. 5b both the experimental data and the theoretical continuous curve present a region with a slope of -4, which is the signature of c-NEFs. In Figs. 5a and b we only show one representative example of the experimental $S(k,t)T(k)$ product from experiment 1a to make sure that it matches the theoretical expressions. Subsequently, in panels Fig. 5c and d we presented one representative example from each experiment without further overlapping them with the theoretically expected curves.

The temporal correlation function, or intermediate scattering function [17], could be a single exponential as in [9, 38, 57, 54]:

$$G(k,t,\Delta t) = e^{-\Delta t/\tau(k,t)}, \qquad (4)$$

where $\tau(k,t)$ is the correlation time of c-NEFs. In some cases, the intermediate scattering function is better fitted by a double exponential [1]. In both our experiments, the intermediate scattering function $G(k,t,\Delta t)$ seemed to be reasonably well approximated by a single exponential. Some representative curves marked with squares (first experiment) and circles (second experiment) are shown in Fig. 6a.

The correlation time, which characterizes the lifetime of concentration fluctuations (see Fig. 6), was fitted with:

$$\tau(k,t) = \frac{1}{Dk^2(1 + (k_c/k)^4)}, \qquad (5)$$

where D is the mass diffusion coefficient. The cutoff wavenumber, k_c, marks the transition between the diffusive and the gravitational regimes (see the vertical dashed line in Fig. 6b). For wavenumbers much larger than the cutoff value k_c, the correlation time in Eq. 5 further reduces to $\tau(k,t) \approx \frac{1}{Dk^2}$. The concentration fluctuations die out due to fast diffusion at small-length scale fluctuations. For wavenumbers
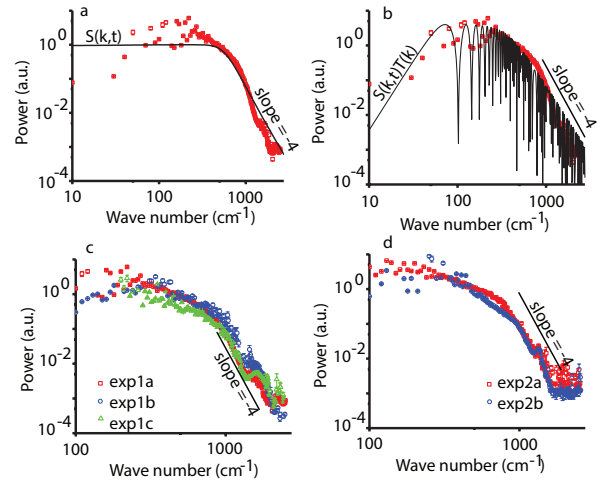

Figure 5: **The experimental and theoretical** $S(k,t)T(k)$ **products.** A log-log plot of a representative estimation from DDA of the experimental $S(k,t)T(k)$ (squares) overlapped with the theoretical curve of the structure factor given by Eq. 3 (continuous line) shows that at large wavenumbers the experimental slope matches the theoretical slope of -4 (a). Some oscillations in the experimental $S(k,t)T(k)$ (squares) could be captured when compared agains the theoretical product of the structure factor given by Eq. 3 by the transfer function from Eq. 2 (continuous curve in panel b). A log-log plot of both the experimental data and the theoretical curve show a region of wave numbers with a power law of -4, which is a signature of giant concentration fluctuations. Additional log-log plots of representative experimental $S(k,t)T(k)$ products are shown in panels c (first experiment) and d (second experiment). The error bars for data fitting were determined with the Levenberg-Marquardt nonlinear curve fitting algorithm.
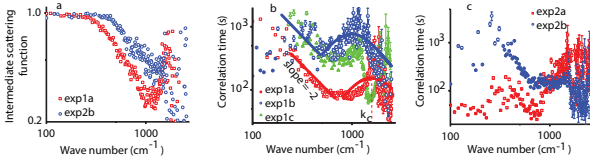
Figure 6: **The intermediate scattering function and the correlation time of fluctuations.** Representative log-log plots of the intermediate scattering function $G(k, t, \Delta t)$ from the first (squares) and second (circles) experiments are shown in panel a. Both experiments seem to be reasonably described by a single exponential function given by Eq.4. The fit of the correlation times $\tau(k, t)$ with the theoretical Eq. 5 are shown in panel b with continue arched curves. The peak of the fitting curve is at the cutoff (critical) wavenumber k_c (see the vertical dashed line in panel b). For small wavenumbers it seems that a new propagation mode that scales with k^{-2} emerges (see the straight continuous lines with slopes of -2). The error bars for data fitting were determined with the Levenberg-Marquardt nonlinear curve fitting algorithm.

smaller than k_c, the correlation time is proportional to k^2 due to the effect of the gravitational force, which for large-size fluctuations becomes the fastest process in the system. As the system is driven towards the homogeneous state by diffusion, the cutoff wavenumber k_c decreases and the maximum correlation time $\tau_{max}(k, t) = \tau_{max}(k_c, t)$ increases. For even smaller wavenumbers, it seems that a propagation mode that scales as k^{-2} emerges (see the straight continue lines in Fig. 6b marked with a slopes of -2). Such modes could be theoretically models as $\tau(k, t) = \frac{2}{\nu k^2}$ where ν is the kinematic viscosity [9], but such modeling is outside the scope of this study (see, for example, [9] for a detailed description of viscosity mode during c-NEFs).

4 Results

The first experiment lasted about 10 hours and it contained three sequences: magnetic field off, then field on, and finally field off again (see the sequence marked "exp 1" in Fig. 1). The second experiment lasted about 6 hours and it contained only two sequences: magnetic field on, and then field off (see the sequence marked "exp 2" in Fig. 1).

For all experiments, the structure functions $C_m(k, t, \Delta t)$ were fitted with Eq. 1 and the correlation function given by Eq. 4. The product of the structure factor $S(k, t)$ by the shadowgraph trans-

fer function $T(k)$ was obtained by direct fitting of the structure function $C_m(k, t, \Delta t)$. The background noise $B(k, t)$ determines the range of wavenumbers for which the signal to noise ratio is too low. In our experiments, the amplitude of the background noise was at least one order of magnitude smaller than the product $S(k, t)T(k)$. Additional pre-processing was done using the variance method as described above in order to further reduce estimations errors [24].

The log-log plot of the experimentally measured $S(k, t)T(k)$ product versus the wavenumber k shows two regions of interest: for small wavenumbers, the structure factor is almost flat, whereas for larger wavenumbers $k > 924 \, \text{cm}^{-1}$ the structure factor can be fitted with a k^{-4} power law in the absence of the external magnetic field (see the solid squares and triangles in Fig. 5c and the solid circles in Fig. 5d). We also found that the experimental data for $S(k, t)T(k)$ (solid squares) overlap with the analytical expression of the product between the theoretical shadowgraph transfer function $T(k)$ and the theoretical structure factor given by Eq. 3 (see Fig. 5a and b).

We also noticed that the slope of the structure factor in the presence of the external magnetic field is between -4 and -3 (see the solid circles in Fig. 5c and the solid squares in Fig. 5d). The low wavenumber region with $k < k_c$ of the experimental $S(k, t)T(k)$ is compatible with the plateau due to the buoyancy effect of gravity, already reported in the literature (see [9] and references therein). The structure factor is almost independent of the wavenumber in this gravitational region.

The log-log plot of the correlation time $\tau(k, t)$ of the c-NEFs has two significant regions of interest (see Fig. 6b and c). At moderate wavenumbers $400 \, \text{cm}^{-1} < k < 924 \, \text{cm}^{-1}$ the gravitational quenching of fluctuations dominates, resulting in an acceleration of the fluctuation lifetimes. At larger wavenumbers, $k > 924 \, \text{cm}^{-1}$, there is a correlation time peak that is related to the diffusion coefficient. At very low wavenumbers $k < 400 \, \text{cm}^{-1}$ a new mode developed that could be related to kinematic viscosity (see [9]), which is outside the goals this study. We fitted this peak in Fig. 6 with Eq. 5 [9] in order to estimate the diffusion coefficient (see Fig. 7a1,a2).

The first part (no magnetic field) of the first experiment served multiple purposes. For example, we used free diffusion as a control experiment allowing us to check the features of giant c-NEFs, e.g. the existence of a scaling law with k^{-4} for the structure factor at large wavenumbers (see Fig. 5). Another reason for this control part of the first experiment was to estimate the diffusion coefficient during the initial duration of the diffusion process after the very long wavelength fluctuations died out [9].
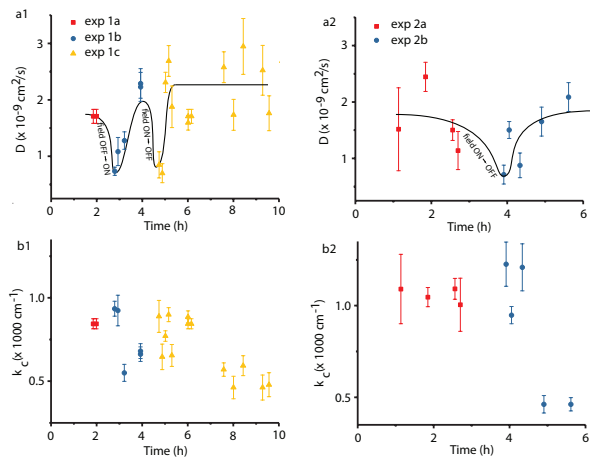
Figure 7: **The diffusion coefficients and the cutoff wave number.** The diffusion coefficients D were determined by fitting the characteristic peaks of the correlation time in Fig. 6 to Eq. 5 (see panels a1 and a2). Each time the magnetic field switches there is a sudden decrease in the diffusion coefficient (see the smooth continuous lines). The cutoff wavenumbers k_c (panels b1 and b2) constantly decrease over time due to the decrease of the concentration gradient.

We expect that similar very long wavelength fluctuations take place at the interface during the first stage of the second experiment. However, the second experiment has a horizontal magnetic field superimposed. There is, however, one caveat regarding the recordings during the first stage in both experiments - based on the variance method (see Fig. 4a) described above (see also [24] for additional details), we have to disregard all recordings of the initial 1-2 hours while the concentration gradient was established. This leaves us with a very small data set for exp 1a and exp 2a (see Fig. 1).

The second stage of the first experiment allows the estimation of the diffusion coefficient after the transient, spurious, very long wavelength fluctuations died out with a superimposed horizontal magnetic field.

Finally, the last stage in both experiments involves only a concentration gradient (no magnetic field). The reason for considering this stage in both experiments is to estimate if there is any remanent effect of the magnetic field on the diffusion coefficient. Although the nanoparticles used in these experiments are on the order of magnitude to exhibit superparamagnetic properties, the demagnetization of the particles is not instantaneous after the removal of the magnetic field.

We hypothesized that in the presence of the external magnetic field (exp 1b and exp 2a in Fig. 1) the

effective "particle" size may become larger than the single-particle size due to the formation of nanorod-like structures. We anticipate that such magnetic field-induced aggregation may reduce the diffusion coefficient. Other mechanisms could contribute to the observed change in diffusion coefficient, such as change in pH, Casimir-like forces, or memory effects (see also the Conclusions section).

From Fig. 7a1 we notice that the diffusion coefficient in the presence of the horizontal magnetic field (see the solid circles that correspond to the values of the diffusion coefficient during the second sequence of the first experiment shown in Fig. 1) starts at lower values than the average diffusion coefficient prior to turning the magnetic field on (see the solid squares that correspond to the first sequence in experiment 1 shown in Fig. 1). A closer look at the diffusion coefficient trend after the horizontal magnetic field was established in the first experiment (Fig. 7a1) suggests that it also steadily increases. By comparing the average diffusion coefficient before the magnetic field against the initial values of the diffusion coefficient with the magnetic field on (solid circles in Fig. 7a1) we notice an initial decrease in the diffusion coefficient when the magnetic field was turned on. We hypothesized that this effect is due to the dampening of the mass diffusion as paramagnetic particles cluster together and increase the effective "particle" size. However, this dampening of the mass diffusion is a transient phenomenon and once the aggregate "particle" size reaches equilibrium value the mass diffusion continues unrestricted. We would have expected that an increased effective particle size would keep the diffusion coefficient lower for the entire duration we hold the magnetic field. The reason such a sustained lower diffusion coefficient did not occur is because the interface fluctuations and the diffusion process take place along the vertical concentration gradient whereas the paramagnetic particles aggregate along the horizontal magnetic field lines. In other words, along the vertical direction of the diffusion process the "particle" size does not change as the paramagnetic particles form horizontal nanorod-like structures.

From the first sequence of the second experiment (see the solid squares in Fig. 7a2) we notice the same transient behavior of the diffusion coefficient when the magnetic field is switched off. We noticed that the diffusion coefficients immediately after the concentration gradient was established have similar values both in the absence (exp 1a) and the presence (exp 2a) of an external horizontal magnetic field.

When finally the horizontal magnetic field is turned off (see sequence 3 in experiment 1 shown in Fig. 7a1 and sequence 2 in experiment 2 shown in Fig. 7a2), initially the diffusion coefficient decreases

again. This is also a transient phenomenon similar to the one that we observe when the magnetic field was established during the previous sequences of the first experiment. This time, the mass diffusion dampening is produced by the breaking of the nanorod-like structures. After a brief transient, the diffusion coefficient increases to a steady value in both experiments.

In addition to the diffusion coefficients, in Fig. 7b1 and b2 shows the evolution of the cutoff wavenumber k_c. Theoretically, the cutoff (critical) wavenumber should continuously decrease as the concentration gradient inside the cell decreases and eventually reach a constant value when the cell is homogeneous [9, 14]. We notice that in the first experiment the cutoff wavenumber decreases over approximately six hours and then reached a constant value when the diffusion stopped (see Fig. 7b1). A similar trend was observed in the second experiment (see Fig. 7b2).

5 Conclusion

We performed two shadowgraph experiments using Fe_2O_3 superparamagnetic nanocolloids with a size distribution between 1-10 nm. Our current results expand previously published data by our team on the effect of a vertical (parallel to the concentration gradient) magnetic field [40]. As in the previous experiments [9, 10, 14, 38], the light source was a low-coherence superluminescent diode and shadowgraph technique was used for estimating nanocolloids' thermophysical properties, such as the diffusion coefficients. In the first experiment, the horizontal magnetic field was applied after the very long wavelength fluctuations dissipated. In the second experiment, the horizontal magnetic field was applied during the initial stage of establishing the concentration gradient when very long wavelength fluctuations take place inside the cell.

In both experiments, the diffusion coefficient begins to increase while under the influence of the magnetic field, presumably due to the fact that the spatial dimension of the nanorod-like structures along the vertical diffusion direction is not affected by the external magnetic field. We also found that when the magnetic field is turned off the diffusion coefficient transiently decreases again, presumably due to the slowing down of the diffusion while the nanorod-like structures break into their composite particles. After this brief transient, the diffusion coefficient increases again while holding the magnetic field.

This behavior of the diffusion coefficient in the presence of a horizontal magnetic field is markedly different from the response to a vertical magnetic field [40]. Indeed, in the presence of a horizontal magnetic

field, it seems that the diffusion coefficient quickly decreases only when we turned on or off the field. In the presence of a vertical magnetic field, we previously found that the diffusion coefficient decreases and remains low during the entire time the magnetic field is present [40].

A possible explanation for a smaller diffusion coefficient when the magnetic field is turned on/off is that the superparamagnetic particles may cluster along the horizontal direction in and external magnetic field. Assuming that our hypothesis is correct, we were able to estimate the length of clusters based on the change in diffusion coefficient. Depending on assumed symmetry of rotation during diffusion, we estimated that the clusters could be from 100 to 9000 particles (see the Appendix for detailed calculations regarding the cluster size).

Although the drop in diffusion coefficient value happens around the time we turned the magnetic field on/off (suggesting a possible magnetic-induced aggregation), we cannot ignore other possible mechanisms that may lead to colloids aggregation. For example, it might be possible that a change in the pH of the colloidal solution produces the observed aggregation of particles [49]. Another possible explanation for the observed change in diffusion coefficient is the existence of giant Casimir-like forces enhanced by non-equilibrium concentration fluctuations [28, 42, 30, 29] that may also lead to nanoparticle clustering. Furthermore, in a similar experiment carried out with highly concentrated (silica) nanocolloids it was found that particle aggregate, possibly due to some non-local and memory effects in dense colloidal suspensions [22]. Taking into consideration the above potential mechanisms for aggregation, we must emphasize that more experiments are needed to discriminate against other potential sources of nanoparticle clustering.

6 Appendix

Thermally induced translational and rotational diffusion are fundamental dynamic processes. For spherical particles, the translational mass diffusion coefficient is given by Stokes-Einstein relation [32]. We used the average diffusion coefficient from the initial ramp of the first sequence in the second experiment (see the solid squares in Fig. 5a1) $D_{avg} = (8.3 \pm 3.6) \times 10^{-10}$ cm^2/s and estimated that the hydrodynamic radius was of the order of $1.6\,\mu m < R < 4\,\mu m$.

The slight decrease of the diffusion coefficient in the presence of an external magnetic field could support the hypothesis that superparamagnetic particles form nanorod-like structures aligned with the ex-

ternal magnetic field. The aggregate of N nanoparticles has a length $L = 2R + 2r(N - 1)$ and a width of $2R$. For diluted colloidal suspensions that may form ellipsoidal aggregates, such as the elongated nanorod-like structures observed in superparamagnetic nanocolloids in external magnetic fields, the translational mass diffusion coefficient is given by [32, 47, 34, 18]:

$$D = \frac{k_B T}{6\pi\eta a} G(\rho),\qquad(6)$$

where a is the semiaxis along the axis of revolution, b are the equatorial semiaxes, and $\rho = b/a$ is the axial ratio. For prolate ellipsoids $\rho < 1$, whereas for oblate ellipsoids $\rho > 1$. The function $G(\rho)$ is given by [32, 47, 34, 18, 27]:

$$G(\rho) = \begin{cases} \frac{1}{\sqrt{1-\rho^2}} Ln\left(\frac{1+\sqrt{1-\rho^2}}{\rho}\right), & \rho < 1 \\ \frac{1}{\sqrt{\rho^2-1}} Arctan(\sqrt{\rho^2 - 1}) & , \rho > 1 \end{cases}$$

$$(7)$$

If the axis of rotation is along the nanorod-like structure, then $a = L = 2R + 2r(N - 1)$, $b = R$ and $\rho = b/a = 1/(2 + 2r(N - 1)/R) < 1$. From Eq. 7 it results that the $2 + 2r(N - 1)/R \approx 6.455$, which means that the average number of magnetic nanoparticles in a cluster is of the order of $N \approx 2.2275R/r$. The largest estimate for $R \approx 4\,\mu m$ and $r = 1$ nm gives about 9000 nanoparticles, which means $9\,\mu m$ long cluster. The smallest estimate is for $R \approx 1.6\,\mu m$ and $r = 10\,nm$, which gives about 360 particles with a total length of almost $3.6\,\mu m$.

The other possibility is that the rotation of the aggregate during diffusion takes place along another axis $a = R$ and $b = L = 2R + 2r(N - 1)$. In this case $\rho = b/a = 2(1 + r(N - 1)/R) > 1$. From Eq. 7 it results that the $2 + 2r(N - 1)/R \approx 3.315$ and the average number of nanoparticles in a cluster is $N \approx 0.6576R/r$. The largest estimate is $N \approx 2600$ particles with a total length of about $2.6\,\mu m$, whereas the smallest number of particles could be $N \approx 100$ for a total length of about $1\,\mu m$.

References:

[1] H Bataller, C Giraudet, F Croccolo, and J M Ortiz de Zarate. Analysis of non-equilibrium fluctuations in a ternary liquid mixture. *Microgravity Science and Technology*, 28(6):611–619, 2016.

[2] C C Berry and A S G Curtis. Functionalisation of magnetic nanoparticles for applications in biomedicine. *Journal of Physics D: Applied Physics*, 36(13):R198, 2003.

[3] P R Bevington. *Data Reduction and Error Analysis for the Physical Sciences*. McGraw-Hill, New York, 1969.

[4] B Bharti, A-L Fameau, M Rubinstein, and O D Velev. Nanocapillarity-mediated magnetic assembly of nanoparticles into ultraflexible filaments and reconfigurable networks. *Nat Mater*, 14(11):1104–1109, 2015.

[5] D Brogioli, F Croccolo, and A Vailati. Correlations and scaling properties of nonequilibrium fluctuations in liquid mixtures. *Phys. Rev. E*, 94:022142, 2016.

[6] D Brogioli, A Vailati, and M Giglio. Universal behavior of nonequilibrium fluctuations in free diffusion processes. *Phys. Rev. E*, 61:R1–R4, 2000.

[7] R Cerbino, S Mazzoni, A Vailati, and M Giglio. Scaling behavior for the onset of convection in a colloidal suspension. *Physical Review Letters*, 94:064501, 2005.

[8] R Cerbino, Y Sun, A Donev, and A Vailati. Dynamic scaling for the growth of nonequilibrium fluctuations during thermophoretic diffusion in microgravity. *Scientific Reports*, 5:14486, 2015.

[9] F Croccolo. *Dynamics of Non Equilibrium Fluctuations in Free Diffusion*. PhD thesis, University of Milano, Milano, 2005.

[10] F Croccolo, H Bataller, and F Scheffold. A light scattering study of non equilibrium fluctuations in liquid mixtures to measure the soret and mass diffusion coefficient. *Journal of Chemical Physics*, 137:234202, 2012.

[11] F Croccolo and D Brogioli. Quantitative fourier analysis of schlieren masks: the transition from shadowgraph to schlieren. *Applied Optics*, 50(20):3419–3427, 2011.

[12] F Croccolo, D Brogioli, A Vailati, M Giglio, and D S Cannell. Effect of gravity on the dynamics of nonequilibrium fluctuations in a free-diffusion experiment. *Annals of the New York Academy of Sciences*, 1077(1):365–379, 2006.

[13] F Croccolo, D Brogioli, A Vailati, M Giglio, and D S Cannell. Use of dynamic schlieren interferometry to study fluctuations during free diffusion. *Appllied Optics*, 45(10):2166–2173, 2006.

[14] F Croccolo, D Brogioli, A Vailati, M Giglio, and D S Cannell. Nondiffusive decay of gradient-driven fluctuations in a free-diffusion process. *Physical Review E*, 76:041112, 2007.

[15] F Croccolo, C Giraudet, H Bataller, R Cerbino, and A Vailati. Shadowgraph analysis of nonequilibrium fluctuations for measuring transport properties in microgravity in the gradflex experiment. *Microgravity Science and Technology*, 28(4):467–475, 2016.

[16] F Croccolo, J M Ortiz de Zarate, and J V Sengers. Non-local fluctuation phenomena in liquids. *European Journal of Physics E*, 39(12):125, 2016.

[17] F Croccolo, F Scheffold, and H Bataller. Mass transport properties of the tetrahydronaphthalene/n-dodecane mixture measured by investigating non equilibrium fluctuations. *Compte Rendu Mecanique*, 341:378, 2013.

[18] P Debye. *Polar Molecules*. Dove Inc., New York, 1929.

[19] J Dobson. Gene therapy progress and prospects: magnetic nanoparticle-based gene delivery. *Gene Ther*, 13:283–287, 2006.

[20] B L Frankamp, A K Boal, and V M Rotello. Controlled interparticle spacing through self-assembly of au nanoparticles and poly(amidoamine) dendrimers. *Journal of the American Chemical Society*, 124:15146–7, 2002.

[21] R A Frimpong and J Z Hilt. Magnetic nanoparticles in biomedicine: synthesis, functionalization and applications. *Nanomedicine*, 5:1401–1414, 2010.

[22] F Giavazzi, G Savorana, A Vailati, and R Cerbino. Simultaneous characterization of

[23] F Giavazzi and A Vailati. Scaling of the spatial power spectrum of excitations at the onset of solutal convection in a nanofluid far from equilibrium. *Physical Review E*, 80:015303, 2009.

[24] C Giraudet, H Bataller, and F Croccolo. High-pressure mass transport properties measured by dynamic near-field scattering of non-equilibrium fluctuations. *Eur. Phys. J. E*, 37(11):107, 2014.

[25] C Giraudet, H Bataller, Y Sun, A Donev, J M Ortiz de Zárate, and F Croccolo. Slowing-down of non-equilibrium concentration fluctuations in confinement. *EPL (Europhysics Letters)*, 111(6):60013, 2015.

[26] P Guenoun, F Perrot, and D Beysens. Microscopic observation of order-parameter fluctuations in critical binary fluids: Morphology, self-similarity, and fractal dimension. *Physical Review Letters*, 63:1152–1155, 1989.

[27] M Hoffmann, C S Wagner, L Harnau, and A Wittemann. 3d brownian diffusion of submicron-sized particle clusters. *ACS Nano*, 3(10):3326–3334, 2009.

[28] T R Kirkpatrick, J M Ortiz de Zarate, and J V Sengers. Nonequilibrium casimir-like forces in liquid mixtures. *Phys. Rev. Lett.*, 115:035901, 2015.

[29] T R Kirkpatrick, J M Ortiz de Zárate, and J V Sengers. Nonequilibrium fluctuation-induced casimir pressures in liquid mixtures. *Phys. Rev. E*, 93:032117, 2016.

[30] T R Kirkpatrick, J M Ortiz de Zárate, and J V Sengers. Physical origin of nonequilibrium fluctuation-induced forces in fluids. *Phys. Rev. E*, 93:012148, 2016.

[31] I Lizarraga, C Giraudet, F Croccolo, M M Bou-Ali, and H Bataller. Mass diffusion and thermal diffusivity of the decane-pentane mixture under high pressure as a ground-based study for scco project. *Microgravity Science and Technology*, 28(545):1–8, 2016.

[32] A Loman, I Gregor, C Stutz, M Mund, and J Enderlein. Measuring rotational diffusion of macromolecules by fluorescence correlation spectroscopy. *Photochem. Photobiol. Sci.*, 9:627–636, 2010.

rotational and translational diffusion of optically anisotropic particles by optical microscopy. *Soft Matter*, 12(31):6588–600, 2016.

[33] S Mazzoni, R Cerbino, A Vailati, and M Giglio. Fluctuations in diffusion processes in microgravity. *Annals of the New York Academy of Sciences*, 1077(1):351–364, 2006.

[34] N Micali, V Villari, M A Castriciano, A Romeo, and L M Scolaro. From fractal to nanorod porphyrin j-aggregates. concentration-induced tuning of the aggregate size. *The Journal of Physical Chemistry B*, 110(16):8289–8295, 2006.

[35] A Oprisan, B Bayley, S A Oprisan, J J Hegseth, Y Garrabos, C Lecoutre, and D Beysens. Thermal fluctuation exponents for two near-critical point systems. *Proc. SPIE*, 7701:77010W–77010W–10, 2010.

[36] A Oprisan, S A Oprisan, B Bayley, J J Hegseth, Y Garrabos, C Lecoutre-Chabot, and D Beysens. Dynamic structure factor of density fluctuations from direct imaging very near (both above and below) the critical point of sf_6. *Phys. Rev. E*, 86:061501, 2012.

[37] A Oprisan, S A Oprisan, J J Hegseth, Y Garrabos, C Lecoutre, and D Beysens. Direct imaging of long-range concentration fluctuations in a ternary mixture. *The European Physical Journal E*, 38(3):1–9, 2015.

[38] A Oprisan, S A Oprisan, and A Teklu. Experimental study of nonequilibrium fluctuations during free diffusion in nanocolloids using microscopic techniques. *Applied Optics*, 49(1):86–98, 2010.

[39] A Oprisan and A L Payne. Dynamic shadowgraph experiments and image processing techniques for investigating non-equilibrium fluctuations during free diffusion in nanocolloids. *Optics Communications*, 290:100–106, 2013.

[40] A Oprisan, A Rice, S A Oprisan, C Giraudet, and F Croccolo. Non-equilibrium concentration fluctuations in superparamagnetic nanocolloids. *The European Physical Journal E*, 40(2):14, 2017.

[41] J M Ortiz de Zárate, J A Fornés, and J V. Sengers. Long-wavelength nonequilibrium concentration fluctuations induced by the soret effect. *Phys. Rev. E*, 74:046305, 2006.

[42] J M Ortiz de Zarate, T R Kirkpatrick, and J V Sengers. Non-equilibrium concentration fluctuations in binary liquids with realistic boundary conditions. *Eur. Phys. J. E*, 38(9):99, 2015.

[43] J M Ortiz de Zárate and J V Sengers. Fluctuations in fluids in thermal nonequilibrium states below the convective rayleigh-benard instability. *Physica A: Statistical Mechanics and its applications*, 300(1-2):25–52, 2001.

[44] J M Ortiz de Zárate and J V Sengers. On the physical origin of long-ranged fluctuations in fluids in thermal nonequilibrium states. *Journal of Statistical Physics*, 115(5):1341–1359, 2004.

[45] J M Ortiz de Zárate and J V Sengers, editors. *Hydrodynamic Fluctuations in Fluids and Fluid Mixtures*. Elsevier, Amsterdam, 2006.

[46] Q A Pankhurst, J Connolly, S K Jones, and J Dobson. Applications of magnetic nanoparticles in biomedicine. *Journal of Physics D: Applied Physics*, 36(13):R167, 2003.

[47] R Pecora. *Dynamic Light Scattering. Applications of Photon Correlation Spectroscopy*. Springer, New York, 1985.

[48] W H Press, S A Teukolsky, W T Vetterling, and B P Flannery. *Numerical Recipes*. Cambridge Univ. Press, New York, 1992.

[49] W B Russel, D A Saville, and W R Schowalter. *Colloidal Dispersions*. Cambridge University Press, Cambridge, 1989.

[50] K D Sattler. *Handbook of Nanophysics: Nanoparticles and Quantum Dots*. Handbook of Nanophysics. CRC Press, 2016.

[51] P N Segre, R W Gammon, and J V Sengers. Light-scattering measurements of nonequilibrium fluctuations in a liquid mixture. *Physical Review E*, 47:1026–1034, Feb 1993.

[52] P N Segre and J V Sengers. Nonequilibrium fluctuations in liquid mixtures under the influence of gravity. *Physica A*, 198:46–77, 1993.

[53] J V Sengers and J M Ortiz de Zárate. Thermal fluctuations in non-equilibrium thermodynamics. *Journal of Non-Equilibrium Thermodynamics*, 32:319–329, 2007.

[54] C J Takacs, A Vailati, R Cerbino, S Mazzoni, M Giglio, and D S Cannell. Thermal fluctuations in a layer of liquid cs_2 subjected to temperature gradients with and without the influence of gravity. *Physical Review Letters*, 106:244502, 2011.

[55] S P Trainoff and D S Cannell. Physical optics treatment of the shadowgraph. *Physics of Fluids*, 14(4):1340–1363, 2002.

[56] A Vailati, R Cerbino, S Mazzoni, M Giglio, G Nikolaenko, C J Takacs, D S Cannell, W M Meyer, and A E Smart. Gradient-driven fluctuations experiment: fluid fluctuations in microgravity. *Appl. Opt.*, 45(10):2155–2165, 2006.

[57] A Vailati, R Cerbino, S Mazzoni, C J Takacs, D S Cannell, and M Giglio. Fractal fronts of diffusion in microgravity. *Nature Communications*, 2(1):290–295, 2011.

[58] A Vailati and M Giglio. Giant fluctuations in a free diffusion process. *Nature*, 390:262–265, 1997.

[59] M Wu, G Ahlers, and D S Cannell. Thermally induced fluctuations below the onset of rayleigh-benard convection. *Physical Review Letters*, 75:1743–1746, 1995.